crystals

MDPI

Article

Spin State Behavior of A Spin-Crossover Iron(II) Complex with N,N′-Disubstituted 2,6-bis(pyrazol-3-yl)pyridine: A Combined Study by X-ray Diffraction and NMR Spectroscopy

Elizaveta K. Melnikova [1,2], Dmitry Yu. Aleshin [1,3], Igor A. Nikovskiy [1], Gleb L. Denisov [1] and Yulia V. Nelyubina [1,*]

1 Nesmeyanov Institute of Organoelement Compounds, Russian Academy of Sciences, Vavilova Str., 28, 119991 Moscow, Russia; elizaveta2198@gmail.com (E.K.M.); dima.aleshin26@gmail.com (D.Y.A.); igornikovskiy@mail.ru (I.A.N.); denisov0gleb@gmail.com (G.L.D.)
2 Lomonosov Moscow State University, Leninskiye gory, 1-3, 119991 Moscow, Russia
3 Mendeleev University of Chemical Technology of Russia, Miusskaya pl., 9, 125047 Moscow, Russia
* Correspondence: unelya@ineos.ac.ru

Received: 26 August 2020; Accepted: 7 September 2020; Published: 8 September 2020

Abstract: A series of three different solvatomorphs of a new iron(II) complex with N,N′-disubstituted 2,6-bis(pyrazol-3-yl)pyridine, including those with the same lattice solvent, has been identified by X-ray diffraction under the same crystallization conditions with the metal ion trapped in the different spin states. A thermally induced switching between them, however, occurs in a solution, as unambiguously confirmed by the Evans technique and an analysis of paramagnetic chemical shifts, both based on variable-temperature NMR spectroscopy. The observed stabilization of the high-spin state by an electron-donating substituent contributes to the controversial results for the iron(II) complexes of 2,6-bis(pyrazol-3-yl)pyridines, preventing 'molecular' design of their spin-crossover activity; the synthesized complex being only the fourth of the spin-crossover (SCO)-active kind with an N,N′-disubstituted ligand.

Keywords: crystallosolvates; iron(II) complexes; molecular design; paramagnetic NMR spectroscopy; spin-crossover; X-ray diffraction

1. Introduction

A renewed interest in long-known [1] spin-crossover (SCO) compounds in the last decades [2] has been boosted by a potential use of their ability to reversibly switch the spin state in response to an external stimulus (such as temperature, pressure, or light irradiation) [3] in displays, sensors, and memory devices [4–8]. Found in many transition metal complexes, the SCO phenomenon in (pseudo)octahedral complexes of iron(II) with an N6 donor ligand set is often sought after [3], with an abrupt switching [9,10] between diamagnetic low-spin (LS) and paramagnetic high-spin (HS) states [11]. Among popular ligands to provide this kind of coordination environment, 2,6-bis(pyrazol-1-yl)pyridines (1-bpp) [12,13] and 2,6-bis(pyrazol-3-yl)pyridines (3-bpp) [14] were a focus of many extensive studies [12,15–18]. For 1-bpp, they resulted in a straightforward recipe [16] for chemical modifications of the ligand to control the SCO behavior of the metal ion. In contrast, complexes of isomeric 3-bpp are severely affected by an environment owing to unsubstituted NH groups that form H-bonds with counterions or solvent molecules [19,20], thus precluding their 'truly molecular' [21] design as SCO compounds.

Until very recently [18], however, any substituent in this position of 3-bpp resulted only in HS complexes of iron(II) mostly [22] through its steric [23] bulk, as generally accepted in the SCO

research [21]. Askew from the common wisdom, the ligand to obtain the first SCO-active complexes of N,N′-disubstituted 3-bpp [18] was created by size-tailoring ortho-substituents in 2,6-functionalized N-phenyl groups. Encouraged by the success, here we report an iron(II) complex of the same ligand design [18] **L** but with a different substituent, an electron-donating bulky t-butyl group, in the fifth position of the pyrazol-3-yl moiety (Scheme 1) to probe its effect on the spin state of the iron(II) ion by two complementary [15] techniques [11,24], X-ray diffraction and NMR spectroscopy. X-ray diffraction is an indispensable tool in search for structure–function relationships [21] in SCO-active complexes [3,17,25], including those of 3-bpp [15], with operative crystal packing forces that may induce a desired abrupt SCO with a thermal hysteresis [9,10] or, instead, 'block' it from occurring [15,26]. The latter makes screening of solutions [21] by NMR spectroscopy, which is behind the popular Evans method [27] or a more exotic analysis [28–32] of paramagnetic chemical shifts [33], crucial for a successful 'truly molecular' design [21] of SCO compounds. Here, both of these techniques are applied for studying the spin-state behavior of the new iron(II) complex of N,N′-disubstituted 3-bpp, $[Fe(\mathbf{L})_2](BF_4)_2$, to get deeper insights into its potential thermally induced SCO [18] ability as a function of chemical modifications of the ligand similar to those gathered for 1-bpp [16].

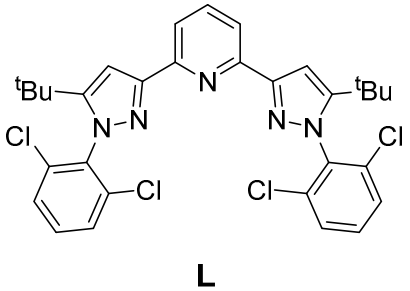

L

Scheme 1. Ligand **L**, 2,6-bis(5-tert-butyl-1-(2,6-dichlorophenyl)-1H-pyrazol-3-yl)pyridine.

2. Materials and Methods

2.1. Synthesis

All procedures were carried out in air and in solvents purchased from commercial sources and purified by distilling from conventional drying agents under an argon atmosphere prior to use. Diethyl 2,6-pyridinedicarboxylate was obtained commercially (Sigma-Aldrich), and 2,6-dichlorophenylhydrazine was synthesized from commercially available 2,6-dichloroanilines using a standard diazotization protocol with a subsequent reduction by $SnCl_2$ [18]. High-resolution mass-spectra were recorded on a Bruker Daltonics microTOF electrospray ionization-time-of-flight (ESI-TOF) mass spectrometer (Bremen, germany).

2.1.1. Synthesis of the Ligand **L**

In the first step, 1,1′-(pyridine-2,6-diyl)bis(4,4-dimethylpentane-1,3-dione) was obtained as described earlier [34] (Scheme 2). To do so, pinacolone (4.36 mL, 35 mmol) was added to a suspension of NaH as a 60% suspension in oil (1.4 g, 35 mmol) and of diethyl 2,6-pyridinedicarboxylate (2.23 g, 10 mmol) in dry THF (100 mL), which was then heated to reflux. After 3 h, the solvent was removed under vacuum, the resulting sodium salt was suspended in water, and the suspension was treated with HCl until the pH value reached 4. The following extraction with $CHCl_3$, drying of the solution with Na_2SO_4, and removal of the solvent in vacuo yielded the target tetraketone as a bright yellow solid, which was of a sufficient purity for further transformations. Yield: 2.51 g (76%). Anal. Calc. for ($C_{19}H_{22}NO_4$): C, 68.48; H, 7.58; N, 4.23. Found: C, 68.34; H, 7.56; N, 4.24. ^{1}H NMR ($CDCl_3$, 400 MHz, 293 K): δ(ppm) = 15.90 (br.s., 2H, 2COH), 8.19 (d., $^3J_{H,H}$ = 7.8 Hz, 2H, m-Py), 7.99 (t., $^3J_{H,H}$ = 7.8 Hz, 1H, p-Py), 7.13 (s., 2H, 2CH), 1.30 (s., 18 H, 2t-Bu). ^{13}C NMR ($CDCl_3$, 101 MHz, 293 K): δ(ppm) = 202.78

(s., C=O), 182.39 (s., COH), 151.86 (s., 2-Py), 138.21 (s., 4-Py), 123.98 (s., 3-Py), 92.59 (s., CH), 39.87 (s., $C(Me)_3$), 27.24 (s., CH_3).

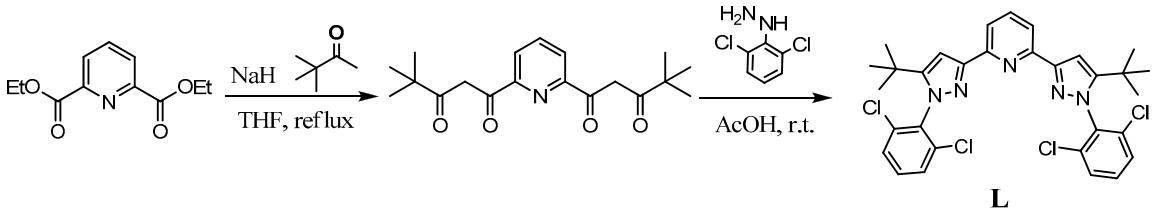

Scheme 2. Synthesis of the ligand **L**.

The ligand **L** (Scheme 2) was synthesized from the obtained 1,1′-(pyridine-2,6-diyl)bis(4,4-dimethylpentane-1,3-dione) (0.331 g, 1 mmol), which was dissolved in 10 mL of acetic acid together with 2,6-dichlorophenylhydrazine (0.407 g, 2.3 mmol) to produce a yellow solution. After its stirring at room temperature overnight, a white precipitate appeared. This precipitate was filtered, washed with acetic acid and water, and dried under vacuum. The product was used without further purification. Yield: 478 mg (78%). Anal. Calc. for ($C_{31}H_{29}Cl_4N_5$): C, 60.70; H, 4.77; Cl, 23.12; N, 11.42 Found: C, 60.62, H, 4.86, N, 11.37. ^{1}H NMR (DMSO-d_6, 400 MHz): δ(ppm) = 7.83 (s., 3H, p-Py + m-Py), 7.76 (d., 4H, $^3J_{HH}$ = 7.9 Hz, m-Ph-H), 7.66 (t., 2H,$^3J_{HH}$ = 7.9 Hz, p-Ph-H), 7.05 (s., 2H, pyraz-CH) 1.24 (s., 18H, t-Bu).^{13}C NMR (THF-d_8, 101 MHz): δ(ppm) = 155.41 (s., 2-Py), 153.89 (s., 5-pyraz), 152.92 (s., 3-pyraz), 139.68 (s., 4-Py), 137.21 (s., 1-Ph), 137.03 (s., 2-Ph), 132.28 (s., 3-Ph), 129.86 (s., 4-Ph), 119.52 (s., 3-Py), 104.56 (s., 4-pyraz), 33.15 (s., $C(Me)_3$), 30.80 (s., CH_3). HR-MS (ESI+), m/z: $[C_{31}H_{29}Cl_4N_5]^+$, calc. 612.1250. found 612.1238.

2.1.2. Synthesis of the Complex $[Fe(L)_2](BF_4)_2$

In a 20 mL vial, iron tetrafluoroborate hexahydrate (0.0337 g, 0.1 mmol) and a ligand **L** (0.122 g, 0.2 mmol) were mixed in 3 mL of acetonitrile and stirred for 1 h. Volatiles were removed under vacuum. For further purification, the solid residue was dissolved in acetonitrile, and diethyl ether was added portion-wise until a precipitate appeared. The mixture was then stored for 12 h at −10 °C. The precipitate was filtered and dried under high vacuum. Yield: 138 mg (95%). Anal. Calc. for ($C_{62}H_{58}B_2Cl_8F_8FeN_{10}$): C, 51.14; H, 4.01; N, 9.62. Found: C, 51.06, H, 3.98, N, 9.54. ^{1}H NMR (CD_3CN, 300 MHz, 285 K): δ(ppm) = 73.54 (br.s., 4H, m-Py-H), 53.67 (br.s., 4H, pyraz-CH), 31.43 (br.s., 2H, p-Py-H), 13.53 (br.s., 4H, p-Ph-H), 10.44 (br.s., 8H, m-Ph-H), -1.42 (br.s., 36H, t-Bu). ^{1}H NMR (CD_2Cl_2, 300 MHz, 290 K): δ(ppm) = 72.90 (br.s., 4H, m-Py-H), 52.87 (br.s., 4H, pyraz-CH), 30.96 (br.s., 2H, p-Py-H), 13.44 (br.s., 4H, p-Ph-H), 10.32 (br.s., 8H, m-Ph-H), −1.22 (br.s., 36H, t-Bu).

2.2. X-ray Crystallography

Single crystals of $[Fe(\mathbf{L})_2](BF_4)_2{\cdot}2CH_3CN$ (red), $[Fe(\mathbf{L})_2](BF_4)_2{\cdot}0.5H_2O$ (red) and $[Fe(\mathbf{L})_2](BF_4)_2{\cdot}2CH_3CN$ (yellow) were grown by slow diffusion of diethyl ether vapor into an acetonitrile solution of this complex kept on air for two months. X-ray diffraction data were collected at 120 K with a Bruker APEX2 DUO CCD diffractometer (Karlsruhe, germany), using the graphite monochromated Mo-Kα radiation (l = 0.71073 Å). For $[Fe(\mathbf{L})_2](BF_4)_2{\cdot}2CH_3CN$ (yellow), they were also collected at 293 K. An attempt to do so for $[Fe(\mathbf{L})_2](BF_4)_2{\cdot}2CH_3CN$ (red) and $[Fe(\mathbf{L})]_2(BF_4)_2{\cdot}0.5H_2O$ (red) was unsuccessful, as heating their single crystals to higher temperatures resulted in their deterioration. Using Olex2 [35], the structures were solved with the ShelXT structure solution program [36] using Intrinsic Phasing and refined with XL refinement package [37] using Least Squares minimization. Hydrogen atoms of water molecules in $[Fe(\mathbf{L})_2](BF_4)_2{\cdot}0.5H_2O$ (red) were located in difference Fourier synthesis. Positions of other hydrogen atoms were calculated, and they all were refined in the isotropic approximation in the riding model. Crystal data and structure refinement parameters for the three crystallosolvates are given in Table 1. CCDC 2021884, 2021885, 2021886, and 2021887 contain the

supplementary crystallographic data for [Fe(**L**)$_2$](BF$_4$)$_2$·2CH$_3$CN (red), [Fe(**L**)$_2$](BF$_4$)$_2$·0.5H$_2$O (red) and [Fe(**L**)$_2$](BF$_4$)$_2$·2CH$_3$CN (yellow) at 120 and 293 K, respectively.

Table 1. Crystal data and structure refinement parameters for [Fe(**L**)$_2$](BF$_4$)$_2$·2CH$_3$CN (red), [Fe(**L**)$_2$](BF$_4$)$_2$·0.5H$_2$O (red) and [Fe(**L**)$_2$](BF$_4$)$_2$·2CH$_3$CN (yellow).

Parameter	[Fe(L)$_2$](BF$_4$)$_2$·2CH$_3$CN (red)	[Fe(L)$_2$](BF$_4$)$_2$·0.5H$_2$O (red)	[Fe(L)$_2$](BF$_4$)$_2$·2CH$_3$CN (Yellow)	
Formula unit	2($C_{62}H_{58}Cl_8FeN_{10}$), 4(BF_4), 4(C_2H_3N)	2$C_{62}H_{58}Cl_8FeN_{10}$, 4BF_4, H_2O	$C_{62}H_{58}Cl_8FeN_{10}$, 2BF_4, 2C_2H_3N	$C_{62}H_{58}Cl_8FeN_{10}$, 2BF_4, 2C_2H_3N
Formula weight	3088.73	2930.52	1538.36	1539.37
T, K	120	120	120	293
Crystal system	Orthorhombic	Monoclinic	Orthorhombic	Orthorhombic
Space group	Pcbn	$P2_1/n$	Fdd2	Fdd2
Z	4	2	8	8
a, Å	45.272(7)	16.9032(12)	42.2980(16)	43.047(14)
b, Å	13.335(2)	21.2547(15)	14.6224(6)	14.742(6)
c, Å	24.665(4)	17.4043(12)	22.9540(9)	23.161(6)
β, °	90	91.033(2)	90	90
V, Å^3	14,890(4)	6251.9(8)	14,197.0(10)	14,699(8)
D_{calc} (g cm^{-1})	1.378	1.557	1.439	1.390
Linear absorption, μ (cm^{-1})	5.58	6.59	5.85	5.65
F(000)	6328	2996	6304	6304
$2\theta_{max}$, °	52	54	54	54
Reflections measured	93,601	66,188	37,118	36,822
Independent reflections	14,645	13,643	7759	8029
Observed reflections [$I > 2\sigma(I)$]	6631	7932	6893	3666
Parameters	938	841	509	474
R1	0.1504	0.0521	0.0341	0.0656
wR2	0.4839	0.1237	0.0776	0.1776
GOF	1.067	0.993	1.024	0.939
$\Delta\rho_{max}/\Delta\rho_{min}$ (e Å^{-3})	1.398/−0.664	0.753/−0.644	0.538/−0.332	0.847/−0.544

2.3. NMR Spectroscopy

^{1}H spectra for the iron(II) complex [Fe(**L**)$_2$](BF$_4$)$_2$ were recorded from its solutions in acetonitrile-d$_3$ and dichloromethane-d$_2$ with Bruker Avance 300 FT-spectrometer (300.15 MHz ^{1}H frequency, Ettlingen, germany). The measurements were done using the residual signals of these solvents (^{1}H 1.94 ppm and 5.32 ppm).

2.3.1. Evans Method

Variable-temperature magnetic susceptibility in acetonitrile-d$_3$ and dichloromethane-d$_2$ was probed by the Evans method [27,38] in the accessible temperature ranges of 235–345 K and 190–300 K, respectively. In all cases, a Wilmad NMR tube equipped with a coaxial insert was used. The inner (reference) tube was filled with the appropriate solvent with approximately 1% of Me$_4$Si, and the outer tube contained the solution of [Fe(**L**)$_2$](BF$_4$)$_2$ (≈1–5 mg/cm^3) in the same solvent with the same concentration of Me$_4$Si. Molar magnetic susceptibility was calculated from the difference between the chemical shift of Me$_4$Si in the pure solvent and its shift in a solution of the complex ($\Delta\delta$ in Hz) in this solvent using the following equation:

$$\chi_M = \frac{\Delta\delta M}{\nu_0 S_f c} - \chi_M^{dia}$$

(M—molar weight of the iron(II) complex, g/mol; ν_0—frequency of the spectrometer, Hz; S_f—shape factor of the magnet ($4\pi/3$); c—concentration of the complex, g/cm^3; $\chi_M{}^{dia}$—molar diamagnetic contribution to the paramagnetic susceptibility calculated using the Pascal's constant [39]). The concentration c was recalculated for each temperature point accounting for the change in the density of the solvent ρ: $c_T = m_s\rho/m_{sol}$, where m_s is the mass of the complex and m_{sol} is the mass of the solution.

2.3.2. Temperature-Dependence of Chemical Shifts

Chemical shifts in ^{1}H NMR spectra from the solutions of $[Fe(\mathbf{L})_2](BF_4)_2$ in acetonitrile-d_3 and dichloromethane-d_2 were analyzed in the accessible temperature ranges of 235–345 K and 190–300 K, respectively. For a compound adopting two different spin states, the observed chemical shift of a given nucleus in the ^{1}H NMR spectrum is a weighted average of those for LS and HS species (η_{LS} and η_{HS} are their populations) given that spin state switching is a fast process in the NMR timescale (which is almost [29] always the case [28]):

$$\delta_{obs} = \eta_{LS}\delta_{LS} + \eta_{HS}\delta_{HS}$$

For the iron(II) complexes with the diamagnetic LS state, this chemical shift (in ppm) can be expressed as:

$$\delta_{obs} = \eta_{LS}\delta_{dia}^{LS} + \eta_{HS}\left(\delta_{dia}^{HS} + \delta_{par}^{HS}\right) \approx \delta_{dia} + \eta_{HS}\delta_{par}^{HS}$$

A good approximation for the diamagnetic contribution δ_{dia}, which is the same for the LS and HS states, is a chemical shift of the same nucleus in the NMR spectrum of a free ligand [40]. Therefore, paramagnetic contribution δ_{par}^{HS} was measured as a difference between the chemical shifts observed for $[Fe(\mathbf{L})_2](BF_4)_2$ and those for the ligand **L**. At high temperatures (T > 200 K), the paramagnetic chemical shifts for a paramagnetic complex with low magnetic anisotropy [33,41] in a pure spin state follow the linear dependence on the inverse temperature (the Curie law): $\delta_{par}^{HS} = A + BT^{-1}$.

2.3.3. Analysis of Theoretical Chemical Shifts

Theoretical chemical shifts in the ^{1}H NMR spectra for $[Fe(\mathbf{L})_2](BF_4)_2$ in acetonitrile-d_3 were obtained as follows: $\delta_{obs} = \delta_{dia} + \delta_{CS} + \delta_{PCS}$. Isotropic paramagnetic (contact) contribution δ_{CS}, which arises from spin polarization conveyed through molecular orbitals, was evaluated with the following equation:

$$\delta^{CS} = \frac{S(S+1)\mu_B}{3kTg_N\mu_N}\cdot g_{iso}\cdot A_{iso}$$

(S—electron spin; g_N—nuclear g-factor; μ_B—Borh magneton; μ_N—nuclear magneton). The g-tensor and isotropic values of hyperfine interaction tensors A_{iso} were taken from quantum chemical calculations [42], using optimized geometry (as described below) of the complex in the HS state. The pseudocontact contribution δ_{PCS}, which arises from dipolar coupling between magnetic moments of a nucleus and of an unpaired electron [43–45], was estimated by fitting the observed chemical shifts to the following equation:

$$\delta_i^{Cal} = \frac{1}{12\pi {r_i}^3}\Delta\chi_{ax}\left(3cos^2\theta_i - 1\right) + \delta_i^{CS} + \delta_i^{dia} \quad (1)$$

(θ_i and r_i—polar coordinates of the nuclei in the coordinate frame of the magnetic susceptibility tensor χ; $\Delta\chi_{ax}$—axial anisotropy of χ).

2.4. Quantum Chemistry

Quantum chemical calculations were performed with the ORCA package, v. 4.2 [46]. Using X-ray diffraction geometries from $[Fe(\mathbf{L})_2](BF_4)_2{\cdot}2CH_3CN$ (red) and $[Fe(\mathbf{L})_2](BF_4)_2{\cdot}2CH_3CN$ (yellow) as a starting point for the following geometry optimization, the geometry of the species $[Fe(\mathbf{L})_2]^{2+}$ was optimized with a TPSSh functional [47,48], which provides good results for the energy difference between the two spin states in (pseudo)octahedral iron(II) complexes [49], and a basis set def2-TZVP [50]. To speed up the calculations, the RIJCOSX approximation [51] with a def2/J fitting basis [52] set was used. Extra tight thresholds for forces and displacements were applied. The solvation effects were included using the Conductor-like Polarizable Continuum Model, as implemented in the ORCA package, v. 4.2 [46], with acetonitrile and water as solvents. The resulting geometry of $[Fe(\mathbf{L})_2]^{2+}$ in the HS state was used to compute g-tensor and isotropic values of hyperfine interaction tensors A_{iso} [42]

with the hybrid PBE0 functional (providing good results for hydrogen spin densities [42] used in calculating chemical shifts in the NMR spectra of paramagnetic compounds) [28] and the basis set def2-TZVP [50].

3. Results and Discussion

For the synthesis of the ligand **L**, a one-step cyclization [34] of 1,1′-(pyridine-2,6-diyl)bis(4,4-dimethylpentane-1,3-dione) and 2,6-dichloro-phenylhydrazine was carried out in glacial acetic acid. Although it could lead to two possible regioisomers with a different location of aryl substituents, only the target isomer, 2,6-bis(5-tert-butyl-1-(2,6-dichlorophenyl)-1H-pyrazol-3-yl)pyridine (**L**), was obtained in a high yield. Its subsequent reaction with $Fe[BF_4]_2{\cdot}6H_2O$ in acetonitrile at room temperature readily produced the iron(II) complex $[Fe(\mathbf{L})_2](BF_4)_2$, as confirmed by elemental analysis and NMR spectroscopy. To characterize it by X-ray diffraction, attempts have been made to grow high-quality single crystals by slow diffusion of diethyl ether vapor into a solution of the complex in acetonitrile. Those resulted in a mixture of red and yellow crystals, the colors of which are indicative [3] of the LS and HS states of the metal(II) ion, respectively, rarely [18] found together in iron(II) complexes with N,N′-disubstituted 3-bpp ligands [21,22,26,53–55]. The X-ray diffraction data collected for them at 120 K (Figure 1) identified three different crystal forms of $[Fe(\mathbf{L})_2](BF_4)_2$ with various lattice solvents, the solvatomorphs $[Fe(\mathbf{L})_2](BF_4)_2{\cdot}2CH_3CN$ (red), $[Fe(\mathbf{L})_2](BF_4)_2{\cdot}0.5H_2O$ (red) and $[Fe(\mathbf{L})_2](BF_4)_2{\cdot}2CH_3CN$ (yellow). The former two with the same color and habitus cannot be distinguished by a naked eye, thus precluding their isolation in quantities needed for other solid-state techniques used in SCO research [24,56], such as variable-temperature magnetochemistry or UV-vis spectroscopy.

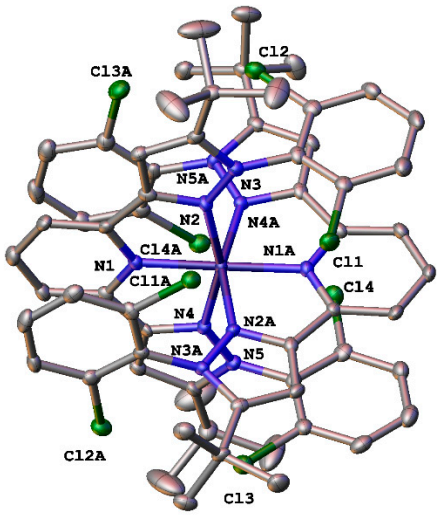

Figure 1. General view of the cation $[Fe(\mathbf{L})_2]^{2+}$ in $[Fe(\mathbf{L})]_2(BF_4)_2{\cdot}0.5H_2O$ (red) from X-ray diffraction at 120 K. Hydrogen atoms are omitted for clarity, non-hydrogen atoms are shown as thermal ellipsoids (p = 50%), and only labels of the heteroatoms in an asymmetric part of the unit cell are given. For other solvatomorphs, see Figures S1 and S2.

Two of the three solvatomorphs, $[Fe(\mathbf{L})_2](BF_4)_2{\cdot}2CH_3CN$ (red) and $[Fe(\mathbf{L})_2](BF_4)_2{\cdot}2CH_3CN$ (yellow) with the complex occupying a general position and a special position (a two-fold axis), respectively, have acetonitrile as a lattice solvent in a complex-to-solvent ratio 1:2. The third one, $[Fe(\mathbf{L})_2](BF_4)_2{\cdot}0.5H_2O$ (red), contains half of a molecule of water, which probably appeared there from keeping the acetonitrile solution of the complex on air. The water molecule is kept in the crystal by OH...F hydrogen bonding with the tetrafluoroborate anions (O...F 2.899(6) and 2.989(6) Å, OHF 148.8(4) and 124.4(4)°); in the other two cases, the latter does not form such bonds due to the absence of suitable H-bond donors. This resulted in a different crystal environment of the complex $[Fe(\mathbf{L})_2](BF_4)_2$ in $[Fe(\mathbf{L})_2](BF_4)_2{\cdot}0.5H_2O$

(red); however, even the solvatomorphs $[Fe(\mathbf{L})_2](BF_4)_2{\cdot}2CH_3CN$ (red) and $[Fe(\mathbf{L})_2](BF_4)_2{\cdot}2CH_3CN$ (yellow) with the same lattice solvent have quite distinct crystal packings.

One of the key features known to play an important role in the solid-state behavior of metal complexes with a potential SCO activity [57] is a 'terpyridine embrace' packing motif [58] arising from face-to-face stacking interactions between neighboring complex species [58,59]. In our case, there are no such motifs in all the three solvatomorphs, although 'terpyridine-embrace'-like patterns can be envisaged in $[Fe(\mathbf{L})_2](BF_4)_2{\cdot}0.5H_2O$ (red) and $[Fe(\mathbf{L})_2](BF_4)_2{\cdot}2CH_3CN$ (yellow) (Figure 2). An overall crystal structure is, however, better described as infinite spirals formed by the cations $[Fe(\mathbf{L})_2]^{2+}$ along the crystallographic axis *a* in $[Fe(\mathbf{L})_2](BF_4)_2{\cdot}2CH_3CN$ (red) and $[Fe(\mathbf{L})_2](BF_4)_2{\cdot}2CH_3CN$ (yellow) and the axis *c* in $[Fe(\mathbf{L})_2](BF_4)_2{\cdot}0.5H_2O$ (red) with the shortest distance between the iron(II) ions equal to 12.900(4), 12.5743(4), and 12.2443(6) Å, respectively. The tetrafluoroborate counterions and appropriate solvent molecules, which are disordered in one of the acetonitrile solvatomorphs, occur between these spirals (Figure 2) to produce a more dense crystal packing in $[Fe(\mathbf{L})_2](BF_4)_2{\cdot}0.5H_2O$ (red) (Table 1) with much smaller solvent cavities [60] occupied by small water molecules [60] and, apparently, more efficient intermolecular interactions favoring the LS state in similar iron(II) complexes [61,62].

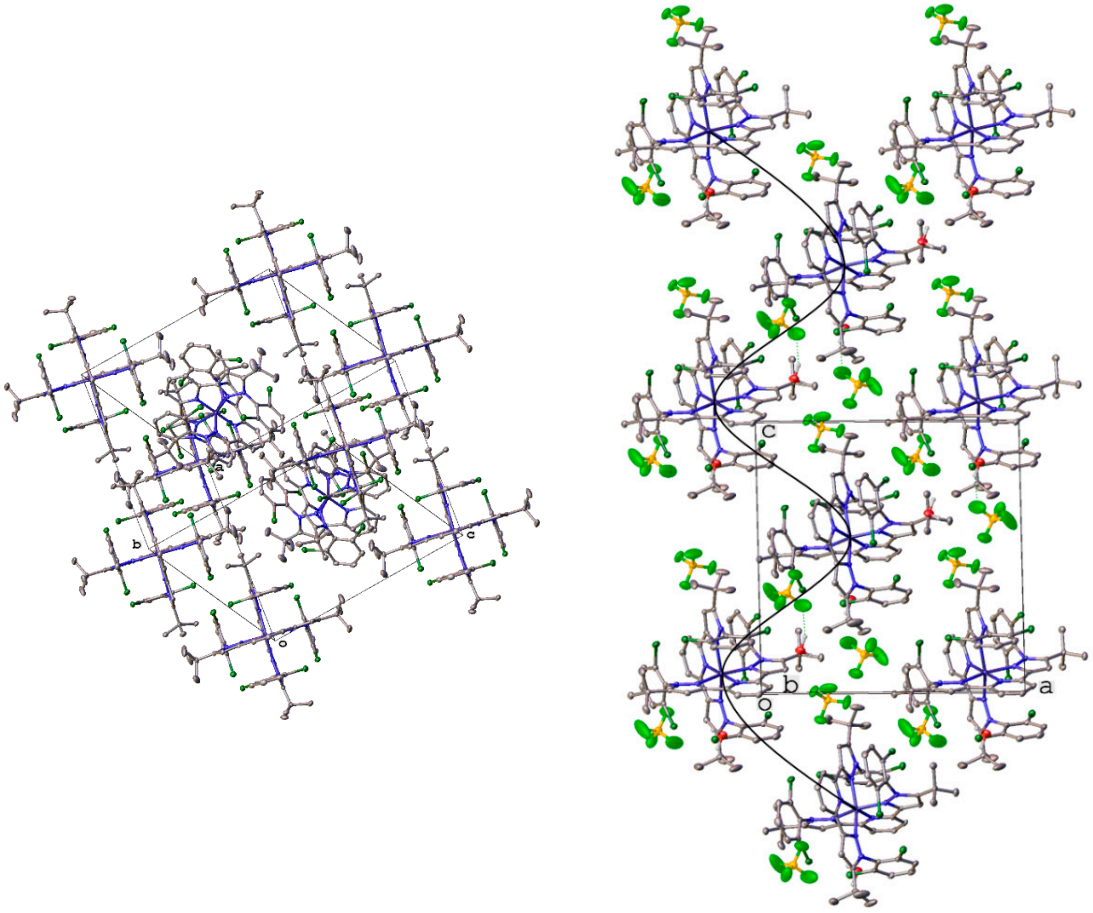

(**a**) (**b**)

Figure 2. 'Terpyridine-embrace'-like (**a**) and spiral-like (**b**) packing of the cations $[Fe(\mathbf{L})_2]^{2+}$ in $[Fe(\mathbf{L})_2](BF_4)_2{\cdot}0.5H_2O$ (red). For other solvatomorphs, see Figures S3 and S4.

The resulting differences in the crystal environment of the cation $[Fe(\mathbf{L})_2]^{2+}$ in the three solvatomorphs are nicely visualized by Hirshfeld surfaces [63,64], which divide the crystal into 'molecular' domains with a dominating contribution to the electron density coming from a particular species, and their 2D fingerprint plots [65], mapping different types of intermolecular interactions and their occurrence by the distances from a point on the Hirshfeld surface to the closest atom inside (d_i)

and outside (d_e) it. Adjusted for the sum of van-der-Waals radii of such pairs of atoms (d_{norm}), these distances allow for color coding the strength of corresponding interactions on the Hirshfeld surface (Figure 3) often shown by red and blue colors for shorter and longer contacts. In the solvatomorphs $[Fe(\mathbf{L})_2](BF_4)_2{\cdot}2CH_3CN$ (red), $[Fe(\mathbf{L})_2](BF_4)_2{\cdot}0.5H_2O$ (red) and $[Fe(\mathbf{L})_2](BF_4)_2{\cdot}2CH_3CN$ (yellow), the Hirshfeld surfaces of the cation $[Fe(\mathbf{L})_2]^{2+}$ all feature intense red areas where they are approached by the tetrafluoroborate anions to produce C–H...F interactions, which appear on the fingerprint plots as most intense areas (Figure 3) contributing 15.3%, 18.4%, and 16.9% to overall crystal packing in $[Fe(\mathbf{L})_2](BF_4)_2{\cdot}2CH_3CN$ (red), $[Fe(\mathbf{L})_2](BF_4)_2{\cdot}0.5H_2O$ (red) and $[Fe(\mathbf{L})_2](BF_4)_2{\cdot}2CH_3CN$ (yellow), respectively. In the two red solvatomorphs, however, there are similar areas close to the solvent molecules in $[Fe(\mathbf{L})_2](BF_4)_2{\cdot}2CH_3CN$ (red) and $[Fe(\mathbf{L})_2](BF_4)_2{\cdot}0.5H_2O$ (red) that form C–H...O and H...H interactions, respectively. The latter are most numerous in the solvatomorphs and account for 55.5%, 60.4%, and 60.3% of the Hirshfeld surface in $[Fe(\mathbf{L})_2](BF_4)_2{\cdot}2CH_3CN$ (red), $[Fe(\mathbf{L})_2](BF_4)_2{\cdot}0.5H_2O$ (red) and $[Fe(\mathbf{L})_2](BF_4)_2{\cdot}2CH_3CN$ (yellow). In all cases, easily recognizable features along the edges of the 2D fingerprint plots are from Cl...H contacts with a contribution of 12.1%, 13.5%, and 11.5%, respectively. Despite many aromatic fragments present in the N,N′-disubstituted 3-bpp ligand **L**, no stacking interactions are observed in $[Fe(\mathbf{L})_2](BF_4)_2{\cdot}2CH_3CN$ (red), $[Fe(\mathbf{L})_2](BF_4)_2{\cdot}0.5H_2O$ (red) or $[Fe(\mathbf{L})_2](BF_4)_2{\cdot}2CH_3CN$ (yellow).

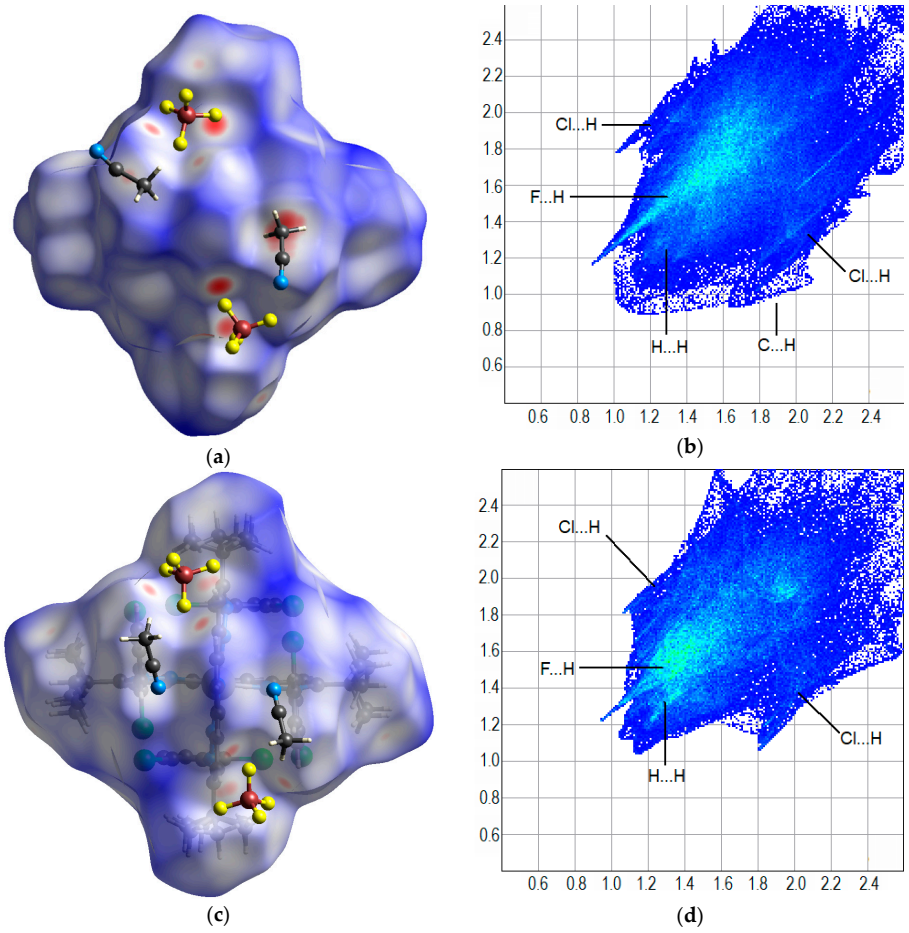

Figure 3. Hirshfeld surfaces of the cation $[Fe(\mathbf{L})_2]^{2+}$ in $[Fe(\mathbf{L})_2](BF_4)_2{\cdot}2CH_3CN$ (red) (**a**) and $[Fe(\mathbf{L})_2](BF_4)_2{\cdot}2CH_3CN$ (yellow) (**c**) and their 2D fingerprint plots (**b**,**d**) as generated by Crystal Explorer [66]. On the Hirshfeld surfaces (**a**,**c**), intermolecular interactions with interatomic distances below, equal or above a sum of van-der-Waals radii are shown by red, white, and blue areas, respectively. green and blue areas on fingerprint plots (**b**,**d**) stand for higher and lower concentration of points corresponding to (di, de) pairs. For the third solvatomorph, see Figure S5.

The different crystal environment of the cation $[Fe(\mathbf{L})_2]^{2+}$ in these solvatomorphs, including those with the same composition ($[Fe(\mathbf{L})_2](BF_4)_2{\cdot}2CH_3CN$ (red) and $[Fe(\mathbf{L})_2](BF_4)_2{\cdot}2CH_3CN$ (yellow)), is clearly behind the different spin state adopted by the metal ion [60], as follows from the colors of these solvatomorphs that are characteristic of LS and HS iron(II) complexes [3], respectively, as well as from X-ray diffraction data collected for them at 120 K (Table 2). Indeed, the Fe-N bond lengths in $[Fe(\mathbf{L})_2](BF_4)_2{\cdot}2CH_3CN$ (red), $[Fe(\mathbf{L})_2](BF_4)_2{\cdot}0.5H_2O$ (red), and $[Fe(\mathbf{L})_2](BF_4)_2{\cdot}2CH_3CN$ (yellow) fall within the ranges typical for, respectively, LS and HS complexes of iron(II) with heterocyclic N-donor ligands [15] that form an N6 coordination environment responding to the spin state of the metal ion [67]. While in the LS state such complexes tend to be octahedral, their HS state is prone to a distortion towards a trigonal prism [68]. For the complexes $[Fe(3\text{-bpp})_2]^{2+}$, it is usually described by the 'twist' angle (θ) between the planes of the two 3-bpp ligands and the 'rotation' angle N_{Py}-Fe-N_{Py} (ϕ) [69]. In any of the three solvatomorphs, these angles are close to 90° and 180° featured by an ideal octahedron (Table 2) and by a previously reported LS solvate with THF [18] of a similar SCO-active iron(II) complex with the hydroxyl groups in the fifth position of the pirazol-3-yl moiety and the same ortho-dichlorophenyl N-substituent. The HS complex $[Fe(\mathbf{L})_2](BF_4)_2$ in $[Fe(\mathbf{L})_2](BF_4)_2{\cdot}2CH_3CN$ (yellow) being only slightly distorted hints on a possibility for an SCO to occur [13].

Table 2. Main geometric parameters [1] and continuous symmetry measures [1] as obtained from X-ray diffraction for $[Fe(\mathbf{L})_2](BF_4)_2{\cdot}2CH_3CN$ (red), $[Fe(\mathbf{L})_2](BF_4)_2{\cdot}0.5H_2O$ (red) at 120 K and for $[Fe(\mathbf{L})_2](BF_4)_2{\cdot}2CH_3CN$ (yellow) at 120 and 293 K.

Parameter	$[Fe(L)_2](BF_4)_2{\cdot}2CH_3CN$ (red)	$[Fe(L)_2]\ (BF_4)_2{\cdot}0.5H_2O$ (red)	$[Fe(L)_2](BF_4)_2{\cdot}2CH_3CN$ (Yellow) 120 K	293 K
Fe-N_{Py}, Å	1.901(12)–1.912(13)	1.910(3)–1.916(3)	2.044(5)–2.046(5)	2.056(9)–2.067(12)
Fe-N_{Pz}, Å	2.025(12)–2.050(9)	2.023(3)–2.032(3)	2.196(3)–2.187(3)	2.202(6)–2.205(7)
θ,°	89.61(11)	89.545(1)	88.882(1)	90.53(9)
ϕ,°	179.4(4)	179.30(12)	180	180.00(4)
γ,°	89.7(5)–90.0 (7) av. 89.85	86.42(13)–89.49(13) av. 88.05	89.94(14)–89.04(13) av. 89.49	88.3(4)–89.0(4) av. 88.65
S(OC-6)	2.599	2.299	3.786	3.819
S(ebcT-6)	13.151	13.485	11.286	11.206

[1] θ is the 'twist' angle between the planes of two 3-bpp ligands; ϕ is the 'rotation' angle N_{Py}-Fe-N_{Py}; γ is the rotation angle of the phenyl group relative to the pyrazol-3-yl plane; S(OC-6) and S(ebcT-6) are octahedral and edge-bicapped tetrahedral symmetry measures, respectively.

A more elegant way to quantify this distortion [67,69], which is often [70] a good indicator of the spin state [26], is to use continuous symmetry measures [67]. They measure how close is the shape of the coordination polyhedron to a reference shape, such as an ideal octahedron (OC-6). The lower the value of an appropriate symmetry measure, the better the fit to a chosen polyhedron is. For example, S(OC-6) would be zero for an ideal octahedron. While an SCO in iron(II) complexes with an N6 donor set is usually associated with a trigonal twist distortion [68], an edge-bicapped tetrahedron (ebcT-6) [69] better matches the coordination environment of the metal ion in HS complexes with two meridian tridentate ligands [69]. For $[Fe(\mathbf{L})_2](BF_4)_2{\cdot}2CH_3CN$ (red), $[Fe(\mathbf{L})_2](BF_4)_2{\cdot}0.5H_2O$ (red), and $[Fe(\mathbf{L})_2](BF_4)_2{\cdot}2CH_3CN$ (yellow), the symmetry measures S(OC-6) and S(ebcT-6) evaluated from the X-ray diffraction data at 120 K (and typical for iron(II) complexes of 3-bpp [26]) clearly distinguish the HS solvatomorph from the two others [26] (Table 2, Figure 4) by the coordination geometry that is more distorted towards an edge-bicapped tetrahedron [69] but hardly enough to prevent an SCO [13,18].

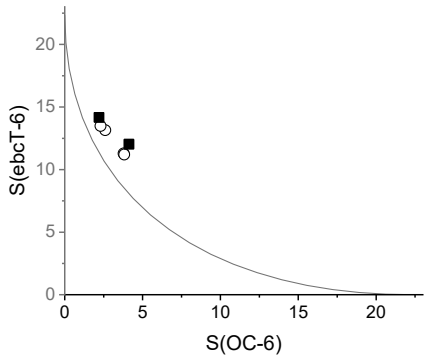

Figure 4. Shape maps for $[Fe(\mathbf{L})_2]^{2+}$. S(OC-6) and S(ebcT-6) are octahedral and edge-bicapped tetrahedral symmetry measures, respectively, with a line representing minimum distortion pathway between these reference shapes. Open circles and black squares correspond to the coordination geometry from X-ray diffraction (Table 2) and quantum chemistry calculations (Table S1), respectively.

Although an SCO-activity in similar iron(II) complexes of 3-bpp with N-aryl substituents [18,22] was previously attributed to the rotation of these substituents from the pyrazol-3-yl plane, an average rotation angle (γ) remains roughly the same in all the three solvatomorphs of $[Fe(\mathbf{L})_2](BF_4)_2$ (Table 2). On the other hand, the rotation angle γ adopts a wider range of values in $[Fe(\mathbf{L})_2](BF_4)_2{\cdot}0.5H_2O$ (red).

The complex $[Fe(\mathbf{L})_2](BF_4)_2$ adopting both the LS and the HS state in the three solvatomorphs (especially those with the same lattice solvent) at the lowest temperature of 120 K available on a diffractometer with our cooling setup suggests a possibility to observe an SCO upon heating. While for $[Fe(\mathbf{L})_2](BF_4)_2{\cdot}2CH_3CN$ (red) and $[Fe(\mathbf{L})_2](BF_4)_2{\cdot}0.5H_2O$ (red), an attempt to collect X-ray diffraction data at higher temperatures failed due to them deteriorating upon heating, for $[Fe(\mathbf{L})_2](BF_4)_2{\cdot}2CH_3CN$ (yellow), they were successfully obtained at 293 K. No SCO, however, occurred in $[Fe(\mathbf{L})_2](BF_4)_2{\cdot}2CH_3CN$ (yellow) with an increase in temperature, as is usually the case of HS complexes; there are, however, some rare examples [71] of an inverse SCO triggered by structural transformations. Heating this solvatomorph of $[Fe(\mathbf{L})_2](BF_4)_2$ to 293 K did not cause any structural changes, as evidenced by the Hirshfeld surface analysis (Figure S6), except for a slight elongation of the bonds Fe-N and a minor decrease in the distortion of the coordination polyhedron towards an edge-bicapped tetrahedron (Table 2). It, however, led to an anisotropic thermal expansion of the unit cell by 3.5%, which is slightly larger than expected for SCO compounds [72]. The lattice parameter ***a*** running along the infinite spirals of the cations $[Fe(\mathbf{L})_2]^{2+}$ (Figure S7) experiences a much larger increase (Figure S8) than the parameters **b** and **c** (18% vs. 8–9%), thus mirroring the changes in the shortest distance between the iron(II) ions in these spirals (from 12.5743(4) to 12.764(3) Å) and between them (from 13.6079(4) to 13.727(3) Å and from 14.6224(6) to 14.742(6) Å in two different directions; Figure S8).

With no color changes upon heating/cooling the crystals of $[Fe(\mathbf{L})_2](BF_4)_2{\cdot}2CH_3CN$ (red), $[Fe(\mathbf{L})_2](BF_4)_2{\cdot}0.5H_2O$ (red) and $[Fe(\mathbf{L})_2](BF_4)_2{\cdot}2CH_3CN$ (yellow), there are no signs of a thermally induced SCO between 120 and 293 K. The different spin state adopted by the iron(II) ion in these solvatomorphs is, apparently, a result of (different) packing forces operating in them that 'lock' the complex $[Fe(\mathbf{L})_2](BF_4)_2$ in one spin state [15,26].

A possibility for it to undergo an SCO decoupled from crystal packing [15,26] or substrate [73,74] effects, such as in solutions [21,33], was supported by quantum chemical calculations of the species $[Fe(\mathbf{L})_2]^{2+}$ in solvents found in the three solvatomorphs (acetonitrile and water), as accounted by the CPCM model [46,75]. The resulting molecular geometries of $[Fe(\mathbf{L})_2]^{2+}$ in the two spin states are close to the experimental ones for $[Fe(\mathbf{L})_2](BF_4)_2{\cdot}2CH_3CN$ (red), $[Fe(\mathbf{L})_2](BF_4)_2{\cdot}0.5H_2O$ (red), and $[Fe(\mathbf{L})_2](BF_4)_2{\cdot}2CH_3CN$ (yellow) (Table 2 and Table S1); the largest difference in the Fe-N bond lengths of 0.085–0.154 Å is observed for the bonds Fe-N_{Pz} in the HS species of the complex. The distortion of the coordination polyhedron towards an edge-bicapped tetrahedron, as quantified by both the 'twist'

and 'rotation' angles and the symmetry measures S(O_h) and S(ebcT) (Table S1, Figure 4), is very similar to that from the X-ray diffraction data collected for the solvatomorphs at 120 K. The orientation of the N-aryl substituents, however, features a larger difference in the rotation angle between the different spin states, which is a key contributor to the spin-state behavior in iron(II) complexes with similar N,N'-aryl-disubstituted 3-bpp ligands [18,22].

The calculated energy difference between the two spin states of $[Fe(\mathbf{L})_2]^{2+}$ is 2.4 kcal/mol, favoring the LS state both in acetonitrile and water media. The latter is in an agreement with the LS state of the iron(II) ion in two out of the three solvatomorphs, with lattice-solvent effects behind its HS state in $[Fe(\mathbf{L})_2](BF_4)_2{\cdot}2CH_3CN$ (yellow) either through [76] geometrical distortions of the iron(II) species or, more likely [13], intermolecular interactions. Such a small difference between the two spin states of $[Fe(\mathbf{L})_2]^{2+}$ additionally hints on a possibility for the complex $[Fe(\mathbf{L})_2](BF_4)_2$ to undergo an SCO but under different conditions, e.g., in a solution.

To observe this hypothetical SCO by the NMR spectroscopy often used [21] for the design of SCO-active compounds [16,21,77–80], a mixture of the solvatomorphs $[Fe(\mathbf{L})_2](BF_4)_2{\cdot}2CH_3CN$ (red), $[Fe(\mathbf{L})_2](BF_4)_2{\cdot}0.5H_2O$ (red), and $[Fe(\mathbf{L})_2](BF_4)_2{\cdot}2CH_3CN$ (yellow) produced by our attempts to grow single crystals of $[Fe(\mathbf{L})_2](BF_4)_2$ was dissolved in acetonitrile-d_3, which provides a good solubility of the complex and occurs in two of the three solvatomorphs. As the popular NMR-based technique in the SCO research [21], the Evans method [27], requires a studied compound to be isolated and thoroughly purified, the mixture was dried under high vacuum to remove the lattice solvents before the sample preparation. ^{1}H NMR spectra collected for the resulting acetonitrile-d_3 solution at the room temperature showed a set of six paramagnetically shifted signals indicative of the complex $[Fe(\mathbf{L})_2](BF_4)_2$ in the HS state.

To assist with the signal assignment, which is sometimes a challenge for the paramagnetic compounds [81], we used an approach [28] successfully applied to various transition metal complexes [81–83], including those with 3-bpp ligands [22,84–86]. At its core is a separation of the chemical shifts for a paramagnetic complex into diamagnetic (δ_{dia}), contact (δ_{cs}) and pseudocontact (δ_{pc}) contributions [45]. The former two are easily obtained from the NMR spectra of the corresponding free ligand [40] and from simple quantum chemical calculations, respectively. To access δ_{pc}, the sum of the three contributions to the chemical shifts δ is fitted to those measured experimentally by varying the value of the magnetic susceptibility tensor anisotropy $\Delta\chi_{ax}$. For $[Fe(\mathbf{L})_2](BF_4)_2$, such a fit resulted in a good match (Figure 5) between the chemical shifts in the ^{1}H NMR spectrum collected from an acetonitrile-d_3 solution of the three (thoroughly dried) solvatomorphs and those estimated by the above approach for the HS species $[Fe(\mathbf{L})_2]^{2+}$ optimized at TPSSh/def2-TZVP level of theory. Together with a reasonable value of $\Delta\chi_{ax}$ expected for the HS iron(II) ion in a (pseudo)coordination environment [45], it confirms the HS state of the complex $[Fe(\mathbf{L})_2](BF_4)_2$ at the room temperature and its only slightly distorted molecular geometry [22] (Table S1) suggestive of a potential SCO [13].

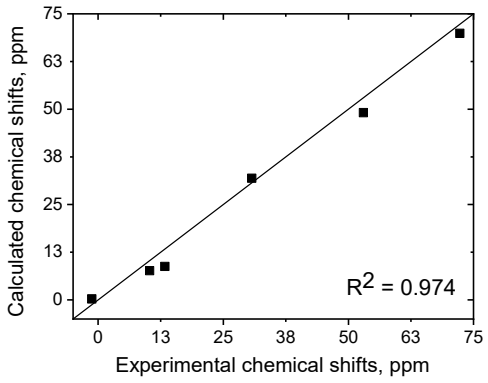

Figure 5. Correlation plot of paramagnetic chemical shifts in the ^{1}H NMR spectrum collected at the room temperature from the solution of $[Fe(\mathbf{L})_2](BF_4)_2$ in acetonitrile-d_3 and those calculated for its high-spin (HS) species with TPSSh-optimized geometry; $\Delta\chi_{ax} = 4.51 \times 10^{-32}$ m^3.

For probing its spin-state behavior upon cooling/heating, the Evans technique [27] is a method of choice [21], as it directly measures the magnetic susceptibility of a solution at different temperatures, which are accessible in a chosen solvent, by comparing chemical shifts of this solvent (or another inert substance, such as TMS) to a pure solvent in the NMR spectra recorded simultaneously. For the complex $[Fe(\mathbf{L})_2](BF_4)_2$ in acetonitrile-d_3, the values χT thus obtained are nearly constant at ≈3.6 cm^3 mol^{-1} K (Figure 6) between 250 and 345 K, thereby corroborating the HS state of the iron(II) in this temperature range. Below 250 K, however, a small decrease in χT is observed down to 3.4 $cm^3mol^{-1}K$, which may signal an onset of an SCO to the diamagnetic LS state. As it may also potentially arise from another well-known drawback of the Evans method [27], the limited accuracy [87] (up to 10% error), an alternative NMR-based approach [33] was used to confirm an SCO by simply following the temperature dependence of the paramagnetic chemical shifts [33] obtained from the same solution of $[Fe(\mathbf{L})_2](BF_4)_2$ as a side-product of the Evans experiment [27]. Relying only on a correct assignment of signals in the NMR spectra, it was successfully applied in a search for new SCO-active compounds among many transition metal complexes [18,28–31,33,41,84,88–90] and even in their mixtures [22,32]. For $[Fe(\mathbf{L})_2](BF_4)_2$, however, the paramagnetic chemical shifts nicely follow a linear dependence on the inverse temperature [22,28,29,89,90] (Figure 6) expected [33,41] for systems in an individual spin state. A very minor deviation from this typical Curie behavior, which may arise from the spin state switching [28], is only hinted at the lowest available temperature in acetonitrile.

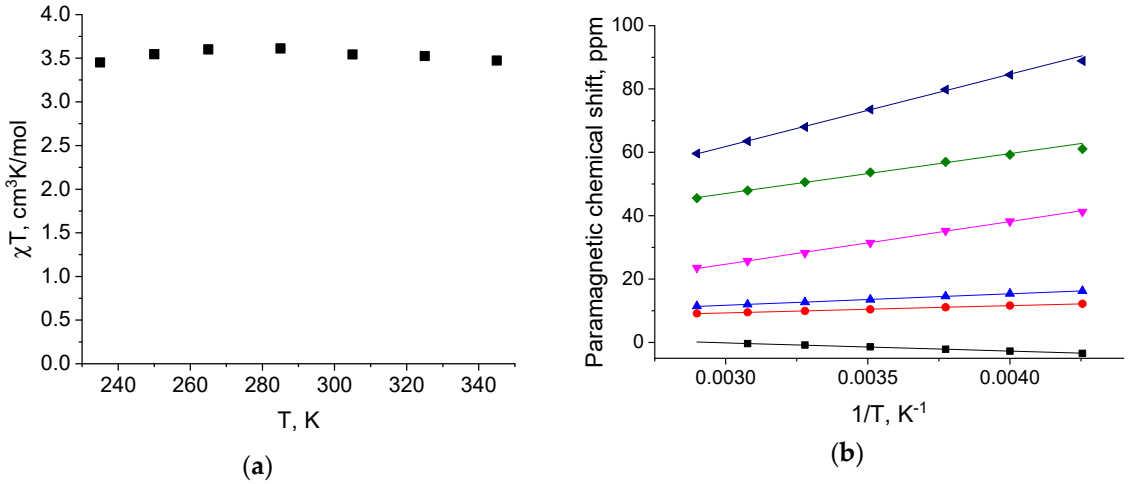

Figure 6. (**a**) Variable-temperature magnetic susceptibility data for the solution of $[Fe(\mathbf{L})_2](BF_4)_2$ in acetonitrile-d_3 according to the Evans method, and (**b**) paramagnetic chemical shifts plotted versus *1/T* (bottom); the lines represent the linear fit over the entire temperature range 250–345 K.

To access lower temperatures, we switched to dichloromethane as another solvent in which the complex $[Fe(\mathbf{L})_2](BF_4)_2$ is soluble, retains its integrity, and produces very similar NMR spectra in an overlapping temperature range of 235–300 K (Figure S9). According to the results obtained by the Evans method [27] for the solution of thoroughly dried solvatomorphs of $[Fe(\mathbf{L})_2](BF_4)_2$ in dichloromethane-d_2, there is indeed an SCO observed upon further cooling (Figure 7), as evidenced by a significant decrease in the χT value down to 2.0 cm^3 mol^{-1} K at 190 K. The latter indicates a gradual population of the diamagnetic LS state, which also follows from a non-Curie behavior of the paramagnetic chemical shifts at the lower temperatures (Figure 7). The corresponding large deviations from the linear dependence [33,41] may only appear from a very fast exchange between the two spin isomers of the SCO-active complex rather than from any other exchange reaction [32] and are, therefore, an unambiguous sign of an SCO occurring in a solution of $[Fe(\mathbf{L})_2](BF_4)_2$ upon its cooling below 250 K. The thermodynamic parameters of this SCO obtained by fitting with a regular solution model [33] are typical for such complexes (Table 3) [16,18,91]. The resulting midpoint temperature (175 K) is, however, much lower than one found in an acetonitrile-d_3 solution of an earlier [18] reported SCO-active iron(II)

complex with hydroxyl groups in the same position of N,N′-disubstituted 3-bpp (269 K [18]). With no crystal packing [15,26] or substrate [73,74] effects operating in both cases, the emerged stabilization of the HS state by the ligand **L** with the t-butyl groups can only be rationalized by the electronic effects of these substituents, as gauged by their Hammett constants [92]. Although an electron-donating t-butyl group in this position of an isomeric ligand, 1-bpp, stabilizes the LS state of the metal ion [16], an opposite trend was sometimes [21,32] observed for the iron(II) complexes of 3-bpp but not confirmed yet, as many of them form H-bonds between their NH groups and counterions/solvents effectively masking the 'molecular' reasons behind the LS/HS stabilization in $[Fe(3\text{-bpp})]^{2+}$ [62,93–96].

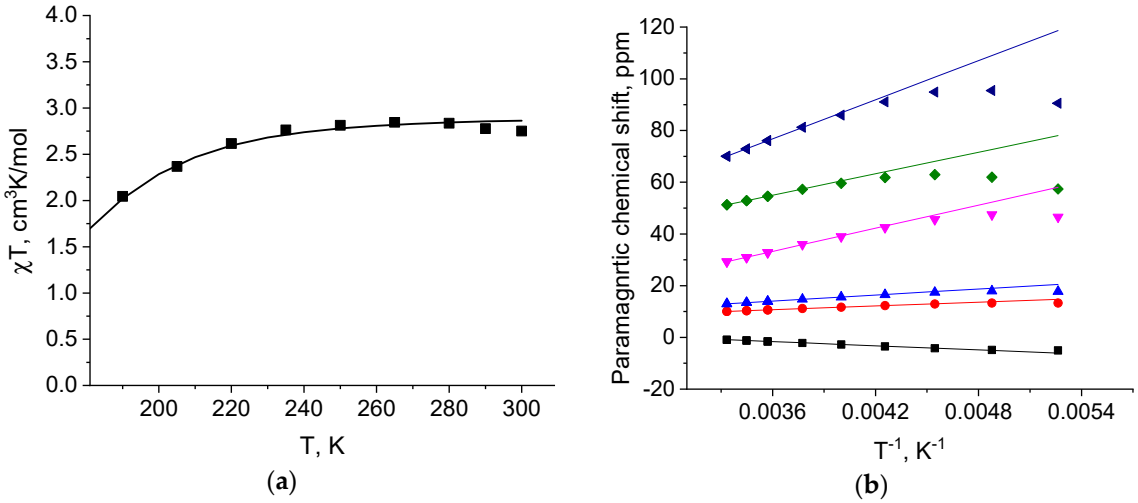

Figure 7. (**a**) Variable-temperature magnetic susceptibility data for the solution of $[Fe(\mathbf{L})_2](BF_4)_2$ in dichloromethane-d_2 according to the Evans method; the line corresponds to the best fit by a regular solution model [33], and (**b**) paramagnetic chemical shifts plotted versus *1/T* (bottom); the lines represent the linear fit over the temperature range 280–300 K.

Table 3. Spin-crossover (SCO) parameters [1] from the NMR data for a dichloromethane-d_2 solution of $[Fe(\mathbf{L})_2](BF_4)_2$.

Parameter	$[Fe(L)_2](BF_4)_2$
$T_{1/2}$, K	175
ΔH, kJ/mol	15.2
ΔS, J/mol	86.9

[1] Thermodynamic parameters are obtained by fitting the Evans data by a regular solution model.

4. Conclusions

In our search for new SCO-active compounds by a combined use of X-ray diffraction and NMR spectroscopy [18,22,32,84–86], an iron(II) complex of N,N′-disubstituted 3-bpp ligands was found to adopt different spin states in a series of three different solvatomorphs $[Fe(\mathbf{L})_2](BF_4)_2{\cdot}2CH_3CN$ (red), $[Fe(\mathbf{L})_2](BF_4)_2{\cdot}0.5H_2O$ (red), and $[Fe(\mathbf{L})_2](BF_4)_2{\cdot}2CH_3CN$ (yellow) as concomitant products of its crystallization in acetonitrile. A variable-temperature NMR study of a solution by the traditional Evans method [27] and by a less popular but more powerful [32] analysis of paramagnetic chemical shifts [33] unambiguously revealed a thermally induced SCO experienced by the complex $[Fe(\mathbf{L})_2](BF_4)_2$ at the lowest temperatures accessible in acetonitrile. The observed stabilization of the HS state by an electron-donating t-butyl group in this position of 3-bpp conflicts with the trend identified for the iron(II) complexes with isomeric 1-bpp [16]. It, however, resonates with the controversial reports on 3-bpp [21,32] mostly resulting from H-bonds between the NH groups of the ligands and counterions/solvent molecules [62,93–96]. They can only be reconciled by a systematic study of

SCO-active complexes with N,N′-disubstituted 3-bpp [18], which is very challenging with $[Fe(\mathbf{L})_2](BF_4)_2$ being only the fourth [18] of this kind.

Supplementary Materials: The following are available online at http://www.mdpi.com/2073-4352/10/9/793/s1, Figure S1: general view of the cation $[Fe(\mathbf{L})_2]^{2+}$ in $[Fe(\mathbf{L})_2](BF_4)_2{\cdot}2CH_3CN$ (red) from X-ray diffraction at 120, Figure S2: general view of the cation $[Fe(\mathbf{L})_2]^{2+}$ in $[Fe(\mathbf{L})_2](BF_4)_2{\cdot}2CH_3CN$ (yellow) from X-ray diffraction at 120 K and 293 K, Figure S3: A fragment of the crystal packing in $[Fe(\mathbf{L})_2](BF_4)_2{\cdot}2CH_3CN$ (red), Figure S4: 'Terpyridine-embrace'-like and spiral-like packing of the cations $[Fe(\mathbf{L})_2]^{2+}$ in $[Fe(\mathbf{L})_2](BF_4)_2{\cdot}2CH_3CN$ (yellow), Figure S5: Hirshfeld surface of the cation $[Fe(\mathbf{L})_2]^{2+}$ in $[Fe(\mathbf{L})_2](BF_4)_2{\cdot}0.5H_2O$ (red) and a 2D fingerprint plot as generated by Crystal Explorer, Figure S6: Hirshfeld surface of the cation $[Fe(\mathbf{L})_2]^{2+}$ and its 2D fingerprint plot for $[Fe(\mathbf{L})_2](BF_4)_2{\cdot}2CH_3CN$ (yellow) at 293 K, Figure S7: Unit cell parameters ***a***, ***b***, and ***c*** of $[Fe(\mathbf{L})_2](BF_4)_2{\cdot}2CH_3CN$ (yellow) at 120 and 293 K, Figure S8: Shortest distances between the iron(II) ions in and between the infinite spirals of the cations $[Fe(\mathbf{L})_2]^{2+}$ in $[Fe(\mathbf{L})_2](BF_4)_2{\cdot}2CH_3CN$ (yellow) at 120 and 293 K, Figure S9: Variable-temperature ^1H NMR spectra for $[Fe(\mathbf{L})_2](BF_4)_2$ in acetonitrile-d_3 and in dichloromethane-d_2, Table S1: Main geometric parameters and continuous symmetry measures as obtained from TPSSh/def2-TZVP calculations of $[Fe(\mathbf{L})_2]^{2+}$ in the LS and the HS state with acetonitrile and water as solvents.

Author Contributions: Conceptualization, Y.V.N.; methodology, E.K.M., D.Y.A., g.L.D. and I.A.N.; software, E.K.M. and g.L.D.; validation, E.K.M., D.Y.A. and g.L.D.; formal analysis, E.K.M.; investigation, E.K.M., D.Y.A., g.L.D. and I.A.N.; resources, Y.V.N.; data curation, Y.V.N.; writing—original draft preparation, E.K.M.; writing—review and editing, Y.V.N.; visualization, E.K.M., g.L.D. and D.Y.A.; supervision, Y.V.N.; project administration, Y.V.N.; funding acquisition, Y.V.N. All authors have read and agreed to the published version of the manuscript.

Funding: This research was supported by the Russian Science Foundation (Project 17-13-01456). Elemental analysis was performed with the financial support from the Ministry of Science and Higher Education of the Russian Federation using the equipment of the Center for molecular composition studies of INEOS RAS.

Conflicts of Interest: The authors declare no conflict of interest.

References

1. Cambi, L.; Szego, L. Uber die magnetische Susceptibilitat der komplexen Verbindungen. *Ber. Dtsch. Chem. Ges.* **1931**, *64*, 2591–2598. [CrossRef]
2. Gütlich, P. Spin Crossover—Quo Vadis? *Eur. J. Inorg. Chem.* **2013**, *2013*, 581–591. [CrossRef]
3. Halcrow, M.A. *Spin-Crossover Materials: Properties and Applications*; John Wiley & Sons, Ltd.: Chichester, UK, 2013.
4. Molnár, G.; Rat, S.; Salmon, L.; Nicolazzi, W.; Bousseksou, A. Spin Crossover Nanomaterials: From Fundamental Concepts to Devices. *Adv. Mater.* **2017**, *30*, 1703862.
5. Senthil Kumar, K.; Ruben, M. Emerging trends in spin crossover (SCO) based functional materials and devices. *Coord. Chem. Rev.* **2017**, *346*, 176–205. [CrossRef]
6. Thorarinsdottir, A.E.; gaudette, A.I.; Harris, T.D. Spin-crossover and high-spin iron(II) complexes as chemical shift 19F magnetic resonance thermometers. *Chem. Sci.* **2017**, *8*, 2448–2456. [CrossRef] [PubMed]
7. Gaudette, A.I.; Thorarinsdottir, A.E.; Harris, T.D. pH-Dependent spin state population and 19F NMR chemical shift via remote ligand protonation in an iron(II) complex. *Chem. Commun.* **2017**, *53*, 12962–12965. [CrossRef] [PubMed]
8. Wang, J.; gondrand, C.; Touti, F.; Hasserodt, J. A pair of highly biotolerated diamagnetic and paramagnetic iron(II) complexes displaying electroneutrality. *Dalton Trans.* **2015**, *44*, 15391–15395. [CrossRef] [PubMed]
9. Brooker, S. Spin crossover with thermal hysteresis: Practicalities and lessons learnt. *Chem. Soc. Rev.* **2015**, *44*, 2880–2892. [CrossRef]
10. Halcrow, M.A. Spin-crossover Compounds with Wide Thermal Hysteresis. *Chem. Lett.* **2014**, *43*, 1178–1188. [CrossRef]
11. Gutlich, P.; garcia, Y.; goodwin, H.A. Spin crossover phenomena in Fe(II) complexes. *Chem. Soc. Rev.* **2000**, *29*, 419–427. [CrossRef]
12. Halcrow, M.A. The synthesis and coordination chemistry of 2,6-bis(pyrazolyl)pyridines and related ligands—Versatile terpyridine analogues. *Coord. Chem. Rev.* **2005**, *249*, 2880–2908. [CrossRef]
13. Halcrow, M.A. Iron(II) complexes of 2,6-di(pyrazol-1-yl)pyridines—A versatile system for spin-crossover research. *Coord. Chem. Rev.* **2009**, *253*, 2493–2514. [CrossRef]
14. Craig, G.A.; Roubeau, O.; Aromí, G. Spin state switching in 2,6-bis(pyrazol-3-yl)pyridine (3-bpp) based Fe(II) complexes. *Coord. Chem. Rev.* **2014**, *269*, 13–31. [CrossRef]

15. Kershaw Cook, L.J.; Mohammed, R.; Sherborne, G.; Roberts, T.D.; Alvarez, S.; Halcrow, M.A. Spin state behavior of iron(II)/dipyrazolylpyridine complexes. New insights from crystallographic and solution measurements. *Coord. Chem. Rev.* **2015**, *289–29*, 2–12. [CrossRef]
16. Kershaw Cook, L.J.; Kulmaczewski, R.; Mohammed, R.; Dudley, S.; Barrett, S.A.; Little, M.A.; Deeth, R.; Halcrow, M.A. A Unified Treatment of the Relationship Between Ligand Substituents and Spin State in a Family of Iron(II) Complexes. *Angew. Chem. Int. Ed.* **2016**, *55*, 4327–4331. [CrossRef]
17. Halcrow, M.A.; Capel Berdiell, I.; Pask, C.M.; Kulmaczewski, R. Relationship between the Molecular Structure and Switching Temperature in a Library of Spin-Crossover Molecular Materials. *Inorg. Chem.* **2019**, *58*, 9811–9821. [CrossRef]
18. Nikovskiy, I.; Polezhaev, A.V.; Novikov, V.V.; Aleshin, D.; Pavlov, A.A.; Saffiulina, E.; Aysin, R.R.; Dorovatovskii, P.; Nodaraki, L.; Tuna, F.; et al. Towards molecular design of spin-crossover complexes of 2,6-bis(pyrazol-3-yl)pyridines. *Chem. Eur. J.* **2020**, *26*, 5629–5638. [CrossRef]
19. Barrett, S.A.; Halcrow, M.A. Anion-dependent spin crossover in solution for an iron(II) complex of a 1H-pyrazolyl ligand. *RSC Adv.* **2014**, *4*, 11240–11243. [CrossRef]
20. Barrett, S.A.; Kilner, C.A.; Halcrow, M.A. Spin-crossover in $[Fe(3\text{-}bpp)_2][BF_4]_2$ in different solvents—A dramatic stabilisation of the low-spin state in water. *Dalton Trans.* **2011**, *40*, 12021–12024. [CrossRef]
21. Halcrow, M.A. The Effect of Ligand Design on Metal Ion Spin State—Lessons from Spin Crossover Complexes. *Crystals* **2016**, *6*, 58. [CrossRef]
22. Nelyubina, Y.V.; Polezhaev, A.V.; Pavlov, A.A.; Aleshin, D.; Savkina, S.A.; Efimov, N.N.; Aliev, T.; Novikov, V.V. Intramolecular Spin State Locking in Iron(II) 2,6-Di(pyrazol-3-yl)pyridine Complexes by Phenyl groups: An Experimental Study. *Magnetochemistry* **2018**, *4*, 46. [CrossRef]
23. Bartual-Murgui, C.; Vela, S.; Darawsheh, M.; Diego, R.; Teat, S.J.; Roubeau, O.; Aromi, G. A probe of steric ligand substituent effects on the spin crossover of Fe(II) complexes. *Inorg. Chem. Front.* **2017**, *4*, 1374–1383. [CrossRef]
24. Gütlich, P.; gaspar, A.B.; garcia, Y. Spin state switching in iron coordination compounds. *Beilstein J. Org. Chem.* **2013**, *9*, 342–391. [CrossRef] [PubMed]
25. Halcrow, M.A. Structure: Function relationships in molecular spin-crossover complexes. *Chem. Soc. Rev.* **2011**, *40*, 4119–4142. [CrossRef] [PubMed]
26. Craig, G.A.; Costa, J.S.; Roubeau, O.; Teat, S.J.; Aromí, G. Local Coordination geometry and Spin State in Novel FeII Complexes with 2,6-Bis(pyrazol-3-yl)pyridine-Type Ligands as Controlled by Packing Forces: Structural Correlations. *Chem. Eur. J.* **2012**, *18*, 11703–11715. [CrossRef]
27. Evans, D.F. The determination of the paramagnetic susceptibility of substances in solution by nuclear magnetic resonance. *J. Chem. Soc.* **1959**, 2003–2005. [CrossRef]
28. Pavlov, A.A.; Denisov, G.L.; Kiskin, M.A.; Nelyubina, Y.V.; Novikov, V.V. Probing Spin Crossover in a Solution by Paramagnetic NMR Spectroscopy. *Inorg. Chem.* **2017**, *56*, 14759–14762. [CrossRef]
29. Petzold, H.; Djomgoue, P.; Hörner, G.; Lochenie, C.; Weber, B.; Rüffer, T. Bis-meridional Fe^{2+} spincrossover complexes of phenyl and pyridyl substituted 2-(pyridin-2-yl)-1,10-phenanthrolines. *Dalton Trans.* **2018**, *47*, 491–506. [CrossRef]
30. Ide, Y.; Murai, N.; Ishimae, H.; Suzuki, M.; Mori, S.i.; Takahashi, M.; Nakamura, M.; Yoshino, K.; Ikeue, T. Spin-crossover between high-spin (S = 5/2) and low-spin (S = 1/2) states in six-coordinate iron(III) porphyrin complexes having two pyridine-N oxide derivatives. *Dalton Trans.* **2017**, *46*, 242–249. [CrossRef]
31. Lin, H.-J.; Siretanu, D.; Dickie, D.A.; Subedi, D.; Scepaniak, J.J.; Mitcov, D.; Clérac, R.; Smith, J.M. Steric and Electronic Control of the Spin State in Three-Fold Symmetric, Four-Coordinate Iron(II) Complexes. *J. Am. Chem. Soc.* **2014**, *136*, 13326–13332. [CrossRef]
32. Pankratova, Y.; Aleshin, D.; Nikovskiy, I.; Novikov, V.; Nelyubina, Y. In Situ NMR Search for Spin-Crossover in Heteroleptic Cobalt(II) Complexes. *Inorg. Chem.* **2020**, *59*, 7700–7709. [CrossRef] [PubMed]
33. Weber, B.; Walker, F.A. Solution NMR studies of iron(II) spin-crossover complexes. *Inorg. Chem.* **2007**, *46*, 6794–6803. [CrossRef] [PubMed]
34. Saalfrank, R.W.; Löw, N.; Trummer, S.; Sheldrick, G.M.; Teichert, M.; Stalke, D. Octanuclear Bis(triple-helical) Metal(II) Complexes. *Eur. J. Inorg. Chem.* **1998**, *1998*, 559–563. [CrossRef]
35. Dolomanov, O.V.; Bourhis, L.J.; gildea, R.J.; Howard, J.A.K.; Puschmann, H. OLEX2: A Complete Structure Solution, Refinement and Analysis Program. *J. Appl. Cryst.* **2009**, *42*, 339–341. [CrossRef]

36. Sheldrick, G.M. SHELXT—Integrated space-group and crystal-structure determination. *Acta Cryst. A* **2015**, *71*, 3–8. [CrossRef]
37. Sheldrick, G.M. Crystal structure refinement with SHELXL. *Acta Cryst. C* **2015**, *71*, 3–8. [CrossRef]
38. Piguet, C. Paramagnetic Susceptibility by NMR: The "Solvent Correction" Removed for Large Paramagnetic Molecules. *J. Chem. Educ.* **1997**, *74*, 815. [CrossRef]
39. Bain, G.A.; Berry, J.F. Diamagnetic Corrections and Pascal's Constants. *J. Chem. Educ.* **2008**, *85*, 532. [CrossRef]
40. Pavlov, A.A.; Nehrkorn, J.; Pankratova, Y.A.; Ozerov, M.; Mikhalyova, E.A.; Polezhaev, A.V.; Nelyubina, Y.V.; Novikov, V.V. Detailed electronic structure of a high-spin cobalt(II) complex determined from NMR and THz-EPR spectroscopy. *Phys. Chem. Chem. Phys.* **2019**, *21*, 8201–8204. [CrossRef]
41. Creutz, S.E.; Peters, J.C. Spin-State Tuning at Pseudo-tetrahedral d^6 Ions: Spin Crossover in $[BP_3]$FeII–X Complexes. *Inorg. Chem.* **2016**, *55*, 3894–3906. [CrossRef]
42. Kaupp, M.; Buhl, M.; Malkin, V.G. *Calculation of NMR and EPR Parameters. Theory and Applications*; WILEY-VCH Verlag gmbH & Co.: Weinheim, 2004.
43. Bertini, I.; Luchinat, C. NMR of Paramagnetic Substances. *Coord. Chem. Rev.* **1996**, *150*, 1–296.
44. Bertini, I.; Luchinat, C.; Parigi, G. Magnetic susceptibility in paramagnetic NMR. *Progr. Nucl. Mag. Res. Spectr.* **2002**, *40*, 249–273. [CrossRef]
45. Bertini, I.; Luchinat, C.; Parigi, G.; Ravera, E. *Solution NMR of Paramagnetic Molecules (Second Edition): Applications to Metallobiomolecules and Models*; Elsevier: Amsterdam, The Netherlands, 2015.
46. Neese, F. Software update: The ORCA program system, version 4.0. *Wiley Interdiscip. Rev. Comput. Mol.* **2018**, *8*, e1327. [CrossRef]
47. Tao, J.; Perdew, J.P.; Staroverov, V.N.; Scuseria, G.E. Climbing the Density Functional Ladder: Nonempirical Meta—Generalized gradient Approximation Designed for Molecules and Solids. *Phys. Rev. Letts* **2003**, *91*, 146401. [CrossRef] [PubMed]
48. Staroverov, V.N.; Scuseria, G.E.; Tao, J.; Perdew, J.P. Comparative assessment of a new nonempirical density functional: Molecules and hydrogen-bonded complexes. *J. Chem. Phys.* **2003**, *119*, 12129–12137. [CrossRef]
49. Cirera, J.; Via-Nadal, M.; Ruiz, E. Benchmarking Density Functional Methods for Calculation of State Energies of First Row Spin-Crossover Molecules. *Inorg. Chem.* **2018**, *57*, 14097–14105. [CrossRef]
50. Weigend, F.; Ahlrichs, R. Balanced basis sets of split valence, triple zeta valence and quadruple zeta valence quality for H to Rn: Design and assessment of accuracy. *Phys. Chem. Chem. Phys.* **2005**, *7*, 3297–3305. [CrossRef]
51. Neese, F. An improvement of the resolution of the identity approximation for the formation of the Coulomb matrix. *J. Comput. Chem.* **2003**, *24*, 1740–1747. [CrossRef]
52. Weigend, F. Accurate Coulomb-fitting basis sets for H to Rn. *Phys. Chem. Chem. Phys.* **2006**, *8*, 1057–1065. [CrossRef]
53. Roberts, T.D.; Little, M.A.; Kershaw Cook, L.J.; Barrett, S.A.; Tuna, F.; Halcrow, M.A. Iron(II) complexes of 2,6-di(1-alkylpyrazol-3-yl)pyridine derivatives—The influence of distal substituents on the spin state of the iron centre. *Polyhedron* **2013**, *64*, 4–12. [CrossRef]
54. Argent, S.P.; Adams, H.; Harding, L.P.; Riis-Johannessen, T.; Jeffery, J.C.; Ward, M.D. Homo- and heteropolynuclear helicates with a '2 + 3 + 2'-dentate compartmental ligand. *New J. Chem.* **2005**, *29*, 904–911. [CrossRef]
55. Barrios, L.A.; Bartual-Murgui, C.; Peyrecave-Lleixa, E.; Le guennic, B.; Teat, S.J.; Roubeau, O.; Aromi, G. Homoleptic versus Heteroleptic Formation of Mononuclear Fe(II) Complexes with Tris-Imine Ligands. *Inorg. Chem.* **2016**, *55*, 4110–4116. [CrossRef] [PubMed]
56. Wolny, J.A.; Schünemann, V.; Németh, Z.; Vankó, G. Spectroscopic techniques to characterize the spin state: Vibrational, optical, Mössbauer, NMR, and X-ray spectroscopy. *Comptes Rendus Chim.* **2018**, *21*, 1152–1169. [CrossRef]
57. Pritchard, R.; Kilner, C.A.; Halcrow, M.A. Iron(ii) complexes with a terpyridine embrace packing motif show remarkably consistent cooperative spin-transitions. *Chem. Commun.* **2007**, 577–579. [CrossRef] [PubMed]
58. Scudder, M.L.; goodwin, H.A.; Dance, I.G. Crystal supramolecular motifs: Two-dimensional grids of terpy embraces in $[ML_2]$ complexes (L = terpy or aromatic N_3-tridentate ligand). *New J. Chem.* **1999**, *23*, 695–705. [CrossRef]

59. McMurtrie, J.; Dance, I. Alternative metal grid structures formed by $[M(terpy)_2]^{2+}$ and $[M(terpyOH)_2]^{2+}$ complexes with small and large tetrahedral dianions, and by [Ru(terpy)2]0. *CrystEngComm* **2010**, *12*, 2700–2710. [CrossRef]
60. Kershaw Cook, L.J.; Kulmaczewski, R.; Cespedes, O.; Halcrow, M.A. Different Spin-State Behaviors in Isostructural Solvates of a Molecular Iron(II) Complex. *Chem. Eur. J.* **2015**, *22*, 1789–1799. [CrossRef]
61. Vela, S.; gourlaouen, C.; Fumanal, M.; Ribas-Arino, J. Disclosing the Ligand- and Solvent-Induced Changes on the Spin Transition and Optical Properties of Fe(II)-Indazolylpyridine Complexes. *Magnetochemistry* **2016**, *2*, 6. [CrossRef]
62. Bartual-Murgui, C.; Codina, C.; Roubeau, O.; Aromí, G. A Sequential Method to Prepare Polymorphs and Solvatomorphs of $[Fe(1,3\text{-bpp})_2](ClO_4)_2{\cdot}nH_2O$ (n = 0, 1, 2) with Varying Spin-Crossover Behaviour. *Chem. Eur. J.* **2016**, *22*, 12767–12776. [CrossRef]
63. McKinnon, J.J.; Mitchell, A.S.; Spackman, M.A. Hirshfeld Surfaces: A New Tool for Visualising and Exploring Molecular Crystals. *Chem. Eur. J.* **1998**, *4*, 2136–2141. [CrossRef]
64. Spackman, M.A.; Jayatilaka, D. Hirshfeld surface analysis. *CrystEngComm* **2009**, *11*, 19–32. [CrossRef]
65. Spackman, M.A.; McKinnon, J.J. Fingerprinting intermolecular interactions in molecular crystals. *CrystEngComm* **2002**, *4*, 378–392. [CrossRef]
66. Wolff, S.K.; grimwood, D.J.; McKinnon, J.J.; Turner, M.J.; Jayatilaka, D.; Spackman, M.A. *CrystalExplorer (Version 3.1)*; University of Western Australia: Perth, Australia, 2012.
67. Alvarez, S. Relationships between Temperature, Magnetic Moment, and Continuous Symmetry Measures in Spin Crossover Complexes. *J. Am. Chem. Soc.* **2003**, *125*, 6795–6802. [CrossRef]
68. Ashley, D.C.; Jakubikova, E. Ray-Dutt and Bailar Twists in Fe(II)-Tris(2,2′-bipyridine): Spin States, Sterics, and Fe–N Bond Strengths. *Inorg. Chem.* **2018**, *57*, 5585–5596. [CrossRef]
69. Alvarez, S. Distortion Pathways of Transition Metal Coordination Polyhedra Induced by Chelating Topology. *Chem. Rev.* **2015**, *115*, 13447–13483. [CrossRef]
70. Kershaw Cook, L.J.; Thorp-Greenwood, F.L.; Comyn, T.P.; Cespedes, O.; Chastanet, G.; Halcrow, M.A. Unexpected Spin-Crossover and a Low-Pressure Phase Change in an Iron(II)/Dipyrazolylpyridine Complex Exhibiting a High-Spin Jahn—Teller Distortion. *Inorg. Chem.* **2015**, *54*, 6319–6330. [CrossRef]
71. Hayami, S.; Komatsu, Y.; Shimizu, T.; Kamihata, H.; Lee, Y.H. Spin-crossover in cobalt(II) compounds containing terpyridine and its derivatives. *Coord. Chem. Rev.* **2011**, *255*, 1981–1990. [CrossRef]
72. Guionneau, P. Crystallography and spin-crossover. A view of breathing materials. *Dalton Trans.* **2014**, *43*, 382–393. [CrossRef]
73. Beniwal, S.; Zhang, X.; Mu, S.; Naim, A.; Rosa, P.; Chastanet, G.; Létard, J.F.; Liu, J.; Sterbinsky, G.E.; Arena, D.A.; et al. Surface-induced spin state locking of the $[Fe(H_2B(pz)_2)_2(bipy)]$ spin crossover complex. *J. Phys. Condens. Mat.* **2016**, *28*, 206002. [CrossRef]
74. Gentili, D.; Liscio, F.; Demitri, N.; Schäfer, B.; Borgatti, F.; Torelli, P.; gobaut, B.; Panaccione, G.; Rossi, G.; Degli Esposti, A.; et al. Surface induces different crystal structures in a room temperature switchable spin crossover compound. *Dalton Trans.* **2016**, *45*, 134–143. [CrossRef]
75. Neese, F. The ORCA program system. *Wiley Interdiscip. Rev. Comput. Mol. Sci.* **2012**, *2*, 73–78. [CrossRef]
76. Fumanal, M.; Jimenez-Gravalos, F.; Ribas-Arino, J.; Vela, S. Lattice-Solvent Effects in the Spin-Crossover of an Fe(II)-Based Material. The Key Role of Intermolecular Interactions between Solvent Molecules. *Inorg. Chem.* **2017**, *56*, 4474–4483. [CrossRef]
77. Phan, H.; Hrudka, J.J.; Igimbayeva, D.; Lawson Daku, L.M.; Shatruk, M. A Simple Approach for Predicting the Spin State of Homoleptic Fe(II) Tris-diimine Complexes. *J. Am. Chem. Soc.* **2017**, *139*, 6437–6447. [CrossRef]
78. Rodríguez-Jiménez, S.; Yang, M.; Stewart, I.; garden, A.L.; Brooker, S. A Simple Method of Predicting Spin State in Solution. *J. Am. Chem. Soc.* **2017**, *139*, 18392–18396. [CrossRef]
79. Kimura, A.; Ishida, T. Spin-Crossover Temperature Predictable from DFT Calculation for Iron(II) Complexes with 4-Substituted Pybox and Related Heteroaromatic Ligands. *ACS Omega* **2018**, *3*, 6737–6747. [CrossRef]
80. McPherson, J.N.; Elton, T.E.; Colbran, S.B. A Strain-Deformation Nexus within Pincer Ligands: Application to the Spin States of Iron(II) Complexes. *Inorg. Chem.* **2018**, *57*, 12312–12322. [CrossRef]
81. Pavlov, A.A.; Nehrkorn, J.; Zubkevich, S.V.; Fedin, M.V.; Holldack, K.; Schnegg, A.; Novikov, V.V. A Synergy and Struggle of EPR, Magnetometry and NMR: A Case Study of Magnetic Interaction Parameters in a Six-Coordinate Cobalt(II) Complex. *Inorg. Chem.* **2020**. [CrossRef]

82. Dudkin, S.V.; Belov, A.S.; Nelyubina, Y.V.; Savchuk, A.V.; Pavlov, A.A.; Novikov, V.V.; Voloshin, Y.Z. Synthesis, X-ray structure and electrochemical properties of hybrid binuclear metallophthalocyaninate-capped tris-pyridineoximates. *New J. Chem.* **2017**, *41*, 3251–3259. [CrossRef]
83. Pavlov, A.A.; Savkina, S.A.; Belov, A.S.; Nelyubina, Y.V.; Efimov, N.N.; Voloshin, Y.Z.; Novikov, V.V. Trigonal Prismatic Tris-pyridineoximate Transition Metal Complexes: A Cobalt(II) Compound with High Magnetic Anisotropy. *Inorg. Chem.* **2017**, *56*, 6943–6951. [CrossRef]
84. Pavlov, A.A.; Aleshin, D.Y.; Nikovskiy, I.A.; Polezhaev, A.V.; Efimov, N.N.; Korlyukov, A.A.; Novikov, V.V.; Nelyubina, Y.V. New Spin-Crossover Complexes of Substituted 2,6-Bis(pyrazol-3-yl)pyridines. *Eur. J. Inorg. Chem.* **2019**, *2019*, 2819–2829. [CrossRef]
85. Pavlov, A.A.; Belov, A.S.; Savkina, S.A.; Polezhaev, A.V.; Aleshin, D.Y.; Novikov, V.V.; Nelyubina, Y.V. Synthesis and Spin State of the Cobalt(II) Complexes with Substituted 2,6-Bis(pyrazol-3-yl)pyridine Ligands. *Russ. J. Coord. Chem.* **2018**, *44*, 489–495. [CrossRef]
86. Pavlov, A.A.; Nikovskii, I.A.; Polezhaev, A.V.; Aleshin, D.Y.; Melnikova, E.K.; Pankratova, Y.A.; Nelyubina, Y.V. Spin State of the Iron(II) and Cobalt(II) 2,6-Di(5-Amino-1H-Pyrazol-3-yl)pyridine Complexes in Solution and in Crystal. *Russ. J. Coord. Chem.* **2019**, *45*, 402–410. [CrossRef]
87. Yatsunyk, L.A.; Walker, F.A. Structural, NMR, and EPR Studies of S = 1/2 and S = 3/2 Fe(III) Bis(4-Cyanopyridine) Complexes of Dodecasubstituted Porphyrins. *Inorg. Chem.* **2004**, *43*, 757–777. [CrossRef]
88. Brunker, T.J.; green, J.C.; O'Hare, D. Electronic Structures of Mixed-Sandwich Complexes of Cyclopentadienyl and Hydrotris(pyrazolyl)borate Ligands with 3d Transition Metals. *Inorg. Chem.* **2003**, *42*, 4366–4381. [CrossRef]
89. Petzold, H.; Djomgoue, P.; Hörner, G.; Speck, J.M.; Rüffer, T.; Schaarschmidt, D. 1H NMR spectroscopic elucidation in solution of the kinetics and thermodynamics of spin crossover for an exceptionally robust Fe^{2+} complex. *Dalton Trans.* **2016**, *45*, 13798–13809. [CrossRef]
90. Petzold, H.; Djomgoue, P.; Hörner, G.; Heider, S.; Lochenie, C.; Weber, B.; Rüffer, T.; Schaarschmidt, D. Spin state variability in Fe^{2+} complexes of substituted (2-(pyridin-2-yl)-1,10-phenanthroline) ligands as versatile terpyridine analogues. *Dalton Trans.* **2017**, *46*, 6218–6229. [CrossRef]
91. Galadzhun, I.; Kulmaczewski, R.; Cespedes, O.; Yamada, M.; Yoshinari, N.; Konno, T.; Halcrow, M.A. 2,6-Bis(pyrazol-1-yl)pyridine-4-carboxylate Esters with Alkyl Chain Substituents and Their Iron(II) Complexes. *Inorg. Chem.* **2018**, *57*, 13761–13771. [CrossRef]
92. Hansch, C.; Leo, A.; Taft, R.W. A survey of Hammett substituent constants and resonance and field parameters. *Chem. Rev.* **1991**, *91*, 165–195. [CrossRef]
93. Scudder, M.L.; Craig, D.C.; goodwin, H.A. Hydrogen bonding influences on the properties of heavily hydrated chloride salts of iron(ii) and ruthenium(ii) complexes of 2,6-bis(pyrazol-3-yl)pyridine, 2,6-bis(1,2,4-triazol-3-yl)pyridine and 2,2′:6′,2″-terpyridine. *CrystEngComm* **2005**, *7*, 642–649. [CrossRef]
94. Clemente-León, M.; Coronado, E.; giménez-López, M.C.; Romero, F.M. Structural, Thermal, and Magnetic Study of Solvation Processes in Spin-Crossover $[Fe(bpp)_2][Cr(L)(ox)_2]_2{\cdot}nH_2O$ Complexes. *Inorg. Chem.* **2007**, *46*, 11266–11276. [CrossRef]
95. Coronado, E.; gimenez-Lopez, M.C.; gimenez-Saiz, C.; Romero, F.M. Spin crossover complexes as building units of hydrogen-bonded nanoporous structures. *CrystEngComm* **2009**, *11*, 2198–2203. [CrossRef]
96. Jornet-Molla, V.; gimenez-Saiz, C.; Romero, F.M. Synthesis, Structure, and Photomagnetic Properties of a Hydrogen-Bonded Lattice of $[Fe(bpp)_2]^{2+}$ Spin-Crossover Complexes and Nicotinate Anions. *Crystals* **2018**, *8*, 439. [CrossRef]